Numerical study of boundary layer interaction with shocks - method and code validation

By N. A. Adams

1. Motivation and objectives

A major problem in modeling of turbulent supersonic flows is the correct assessment of viscous-inviscid interaction problems. Of particular interest is the interaction of boundary layers with shocks. Present turbulence models give in most cases unsatisfactory results in the region of rapid distortion and in the separation region (if one is present) in particular with regard to mean flow profiles and turbulence quantities (cf. Kline *et al.*, 1981).

Recent direct numerical simulations (DNS) at moderate supersonic Mach numbers of boundary layers without interaction show that the effect of compressibility in those cases is rather small (Guo & Adams, 1994). Even at those Mach numbers, however, compressibility can have a significant effect in case viscous-inviscid interaction is present.

Compression corner flows are of great practical interest since they appear to be omnipresent in aeronautical configurations (aircraft fuselage, fuselage-wing junction, engine inlet, etc.). On the other hand, they also give rise to a particularly interesting combination of phenomena, which all are more or less confined to a relatively narrow region about the corner. First, the turbulence in the oncoming boundary layer responds to a rapid distortion. This is a generalization of the problem of isotropic turbulence interacting with normal shocks (e.g. Lee, 1993) to anisotropic turbulence with inhomogeneous mean shear. Second, for large enough Mach numbers and deflection angles there is a shock-induced unsteady separation. The separation bubble is contained by a detached curved shear layer, and fluctuations in this shear layer, subject to high strain, are strongly amplified. Some experiments report evidence for Görtler-like vortices in the detached shear layer (Smits & Muck, 1987). Third, there is unsteady shock motion, which is suspected to be triggered by bursting events in the oncoming turbulent boundary layer (Andreopoulos & Muck, 1987). And finally, the shock is generated at the wall. This is favorable for direct numerical simulations since it relieves the need to accurately introduce a shock at the outer boundaries.

The objective of the present work is the direct numerical simulation of shock boundary layer interaction. This report summarizes the first phase during which a numerical method suitable for this problem has been developed and a computer code has been written and tested.

2. Accomplishments

The first part of this work focuses on the development of a new type of spatial discretization scheme which combines the spectral-like wave-representation of symmetric compact finite difference schemes (Lele, 1992) with a suppression of aliasing

errors by implicit dissipation at non-resolved wavenumbers and increased robustness against generation of spurious waves at the boundaries. In an additional step the scheme is made shock capturing by switching locally to an essentially non-oscillatory (ENO) scheme near discontinuities (in case of weak solutions). In this report the numerical method is merely outlined; for details the reader is referred to Adams & Shariff (1994).

The newly developed spatial scheme is used to discretize the reduced hyperbolic part of the Navier-Stokes equations while for the parabolic part a symmetric compact finite difference scheme is used (cf. Adams, 1993). This report summarizes the status after implementation and validation of the according computer code.

The performance of the present working code lies in between about 200 MFLOPS and about $140\mu s$ per grid point and time step (pure 3rd order ENO, 2D) and about 500 MFLOPS and roughly $20\mu s$ per grid point and time step (pure compact-FD, 3D) on a single CRAY Y-MP C90 CPU. These relations reflect the increased number of logical instructions required for the non-linear ENO scheme.

2.1 Numerical method

Generalizing the formulation of compact finite-difference schemes (Lele, 1992), a family of centered upwind-biased compact schemes of 5th order is introduced. Numerical dissipation is used to suppress unresolved wavenumbers while an accurate representation of the dispersion relation for resolved wavenumbers is required. This requirement is formulated as a constrained optimization problem. A parameter study allows for the generation of a whole family of locally optimal schemes, one member of which, called P455/1, we are using in this study. The general formula of the schemes is

$$\sum_{\mu=-\mu_l}^{\mu_r} \alpha_\mu f_{j+\mu}^{(\sigma)} = \frac{1}{h^\sigma} \sum_{\nu=-\nu_l}^{\nu_r} a_\nu f_{j+\nu} \,. \tag{1}$$

In this equation $f_j = f(x_j)$ is the grid function, the derivative of order σ of which is searched for. For scheme P455/1 it is $\sigma = 1$, $\mu_l = \mu_r = \nu_l = \nu_r = 2$ for interior schemes, $\mu_l = \nu_l = 1$, $\mu_r = 2$, $\nu_r = 3$ for the left next-to-boundary scheme and $\mu_l = \nu_l = 0$, $\mu_r = 2$, $\nu_r = 4$ for the left boundary scheme (accordingly for the schemes at the right boundary). The coefficients α_μ and a_ν are determined from order conditions and the abovementioned optimization problem. For the numerical values see Adams & Shariff (1994).

The discrete derivative operator for a semi-discretized scalar advection equation on a strip consists of interior and boundary schemes whose frequency responses are shown in Fig. 1. It should be noted that the dispersion, Fig. 1a, is well approximated up to wavenumbers larger than 2, significantly increasing the resolved-wavenumber domain when compared with non-compact finite-difference schemes (e.g. that of Rai & Moin, 1993). The numerical dissipation is shown in Fig. 1b.

Moreover, the compact formulation allows for stable high-order boundary closures avoiding the order-drop at the boundary as in Rai & Moin (1993). Note that it has been shown by Gustafsson (1975) that for hyperbolic equations the boundary closures must not be of order less than $(r-1)$ to maintain a global order r of

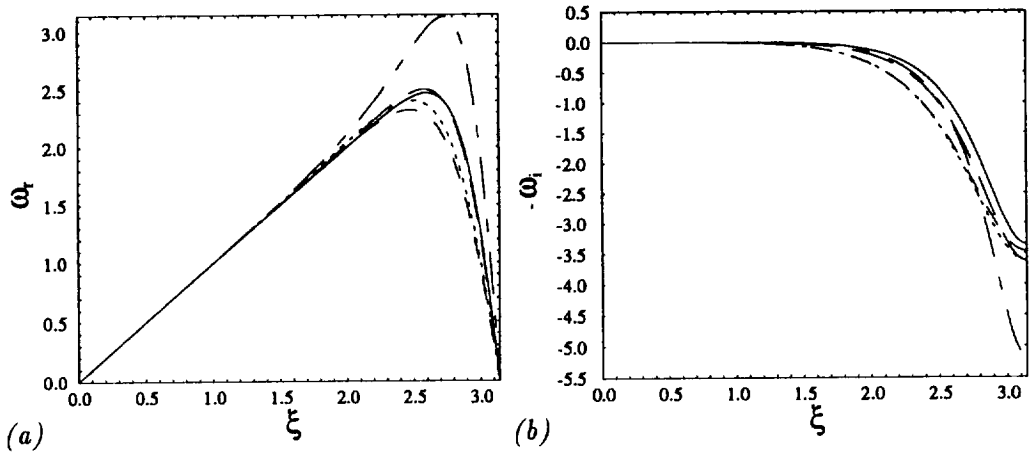

FIGURE 1. Frequency response ω_r of scheme P455/1, (a) real part, (b) imaginary part.····· scheme at left boundary; ---- scheme next to left boundary; ——— interior scheme; -·- scheme at right boundary; —— scheme next to right boundary. ξ is the wavenumber normalized with the grid spacing.

the semidiscretization. The linear stability of this scheme is analyzed in Adams & Shariff (1994).

Two different approaches of making an underlying compact scheme shock capturing (nonlinearly stable) have been pursued initially. The first followed the approach of Cockburn & Shu (1994), which required some minor modifications to be applicable for our general type of upwind compact schemes. Numerical tests, however, showed an unsatisfactory shock resolution. A Gibbs-like phenomenon could not be suppressed satisfactorily without a significant smearing of the shock. The second follows the guideline of Hou & Le Floch (1994), who gave evidence that a nonconservative scheme converges to a weak solution (so a solution exists) if in the neighborhood of discontinuities a conservative scheme is used. In our case scheme P455/1 is used in the smooth regions, while a 5th order ENO scheme in finite-difference form (Shu & Osher, 1989) using Roe fluxes on local characteristics with entropy-fix by switching to a local Lax-Friedrichs flux formulation is used near discontinuities. Without being able to give theoretical evidence, numerical tests reported in Adams & Shariff (1994) demonstrate that the hybrid scheme possesses the ENO property.

For integration in time two different 3rd order Runge-Kutta methods are used. A pure ENO scheme as spatial discretization is combined with a TVD Runge Kutta scheme (Shu, 1988). The hybrid scheme is combined with a low-storage explicit Runge Kutta scheme (Williamson, 1980, case 7). The admissible time step is calculated from an estimated bound for the discrete convective and the discrete viscous operator using a CFL (Courant-Friedrichs-Lewy) condition.

2.2 Discretization of the compressible conservation equations

The fundamental equations are the volume-specific conservation equations for

mass momentum and energy

$$\frac{\partial \mathbf{U}}{\partial t} = \frac{\partial \mathbf{F}}{\partial x} + \frac{\partial \mathbf{G}}{\partial y} + \frac{\partial \mathbf{H}}{\partial z} + \mathbf{Z} \,. \tag{1}$$

The flux vectors **F**, **G**, and **H** are given, for example, in Anderson *et al.*(1984). The viscosity μ is calculated from Sutherland's law. **Z** is a distributed forcing which can be used to cancel the residual of a given basic flow (this is done in the calculations of sections 2.4.1 and 2.4.2, otherwise $\mathbf{Z} = 0$). For a discussion of this term see, for instance, Adams (1993).

The fundamental systems of PDE are discretized in a method of lines manner, i.e. the spatial derivatives of the fluxes are approximated by a spatial discretization. The system thus becomes an ODE in t in terms of the grid point values and is projected forward in time with a Runge-Kutta integration method.

The viscous fluxes are discretized in conservative form by a symmetric P346-scheme used in Adams (1993). Note that although a conservative discretization of a linear heat equation with this scheme would be asymptotically unstable (Adams, 1993), this kind of discretization remains bounded in the present case with an upwind discretization of the convective terms. Since a conservative discretization has significantly less operations, it has been given the preference over the non-conservative discretization used in Adams (1993).

The discretization of the convective terms has been a major objective. For the details the reader is referred to Adams & Shariff (1994). Here, it is summarized in a few words. At each t the fluxes calculated from the instantaneous solution are processed by a discontinuity detector algorithm, and cells are marked for treatment by the ENO scheme. In the present code this is done in each index space component, and a whole plane is marked if at least one cell of this plane contains a transition. This is favorable for vectorization but has the disadvantage that the ENO scheme may be used in smooth regions, too. For the marked cells the fluxes are projected on the local characteristics by a transformation with the left-eigenvector modal matrix of the cell's Roe matrix. The flux derivatives at the cell faces (i.e. the nodes) are reconstructed from the cell-centered numerical fluxes on local characteristics obtained with a 5th order ENO scheme using a Roe-flux formulation with a local Lax-Friedrichs flux as entropy fix. The numerical fluxes (after application of the ENO procedure) are then projected back onto the computational space basis by a transformation with the corresponding right-eigenvector modal matrix.

The flux derivatives in the smooth regions are calculated with the positive biased and the negative biased compact schemes. This is done by projecting the fluxes with the respective right-hand side matrices of the schemes onto a local average, where the entries at the grid points at which the solution is to be taken from the ENO procedure are replaced with the already known flux derivatives. The left-hand side is modified accordingly by setting the respective submatrix to unity. In the reconstruction step the so obtained linear equation systems (pentadiagonal) are solved for the positive and negative biased fluxes. The upwinding is done by choosing the flux derivative in upwind direction according to the direction of the local

characteristics at each grid point. In case of a vanishing eigenvalue, the arithmetic mean is taken as is for the flux derivatives obtained by ENO since they are already upwinded. The advantage of this non-building block (though straight forward) flux splitting is that the flux-approximation is smooth up to the order of the scheme at sonic points. This would not be the case in general if split fluxes would be used.

2.3 Outflow boundary treatment

A major concern of direct numerical simulation methods for spatially evolving convective problems is the correct formulation at the outflow boundary. Since this boundary is artificial a prescription of the correct conditions would require the knowledge about the solution at this plane. Several approaches are now in more or less standard use. For incompressible flows there is the relaminarization method of Kloker *et al.*(1993). In compressible flow Pruett *et al.*(1994) use a buffer domain approach. Guo *et al.*(1994) suggested a much simpler method with the same efficiency as the buffer domain approach. In this work we adopt the latter, though in a different formulation, to account for the non-perturbation form of the equations solved here since the basic flow residual is not compensated by a forcing term as in Pruett *et al.*, 1994, and Guo *et al.*, 1994. Simpler approaches, for instance non-reflecting conditions (e.g. Poinsot & Lele, 1992), treat viscous wave forms within the boundary layer improperly and give rise to spurious reflected waves.

The basic idea follows closely the concept of a *sponge layer* according to Israeli & Orszag (1981). From a simple model equation as

$$\frac{\partial v}{\partial t} = \frac{\partial v}{\partial x} - \sigma(x)v \tag{2}$$

it is seen that $\sigma(x)$ in the last term of the right-hand side has the character of a *Newtonian cooling* coefficent.

We choose the following damping function (cf. Israeli & Orszag, 1981)

$$\sigma(x) = A_s(N_s+1)(N_s+2)\frac{(x-x_s)^{N_s}(L_x-x)}{(L_x-x_s)^{N_s+2}} \tag{3}$$

for $x_s < x \leq L_x$. It has the properties: (i) $\int_{x_s}^{L_x} \sigma(x)dx = A_s$ and (ii) $\sigma(L_x) = 0$.

The implementation is done readily by adding a term

$$\mathbf{Z}_s = -\sigma(x)(U - U_0)$$

for $x_s < x \leq L_x$ to the fundamental equations (1). Herein U denotes the vector of conservative variables and $U_0 = U|_{t=0}$. From property (ii) of σ it is clear that the fundamental equations (1) are recovered at $x = L_x$ where a perfect non-reflecting condition is prescribed (Thompson, 1987).

2.4 Code validation

The computer code is validated using two kind of tests. The first is typical for DNS codes where a known mean flow is enforced and the correct representation of a

TABLE 1. Flow parameters.

Case	M_∞	Re_{δ_1}	T_w/T_∞	α	β	L_z
A	2.5	12773	2.041	0.26	0.43	15
B	4.5	10000	4.38	2.25	0	10

linear eigensolution is required. The second is typical for CFD codes where a mean flow is to be found.

In the first case we check for the efficiency and correct implementation of derivative and integration routines by marching eigensolutions of a temporally evolving boundary layer (streamwise periodic) in time. The global growth rate (defined from the mode energy Eq. (4)) is required to match the real part of the eigenvalue. Also, since the amplitude function is only a function of the wall normal coordinate z, frequency and growth rate at a given z should be close to the imaginary and real part of the eigenvalue locally in z. Inflow and outflow boundary conditions are examined by considering spatial instability in a parallel boundary layer. The spatial growth rate is required to be sufficiently accurately represented and the outflow boundary condition should have a limited upstream effect.

In the second test the steady problem of a shock impinging on a flat plate boundary layer is investigated. Though none of the methods used here is suitable to obtain steady state solutions efficiently, evidence is given that the (quasi time dependent) solution marches toward a steady state. After a reasonable number of iterations the computations are halted and compared with reference data.

2.4.1 Eigensolutions of temporally evolving boundary layer

As test cases we choose cases B and C from Adams (1993, section 6.1). For completeness the flow parameters are given in table 1. A combined algebraic-*sinh* mapping is used in z; see Adams, 1993, section 6.1 for parameters. Boundary conditions are periodic in x and y, non-reflecting at $z = L_z$, and isothermal no-slip at the wall with the wall temperature set to the adiabatic wall temperature (Mack, 1984).

The unperturbed mean flow is calculated from the compressible similarity equations (Stewartson, 1964) with a shooting method (Adams, 1993). An unstable eigenmode with streamwise and spanwise wavenumbers α and β, respectively, as given in table 1 calculated from a spectral solution method (Simen, 1993) (used earlier in Adams, 1993) is superimposed. For case A the eigensolution is an oblique vortical mode, for case B a two dimensional Mack mode (mixed vortical/acoustic). In both cases the initial amplitude is $A = 10^{-4}$. The grid spacing in x and y is uniform, the box dimensions are chosen consistently with the wavenumbers such that the eigenmodes become $(\pm 1, \pm 1)$ and $(\pm 1, 0)$ Fourier modes, respectively.

For the calculations scheme P455/1 is used. Since the solution is smooth the

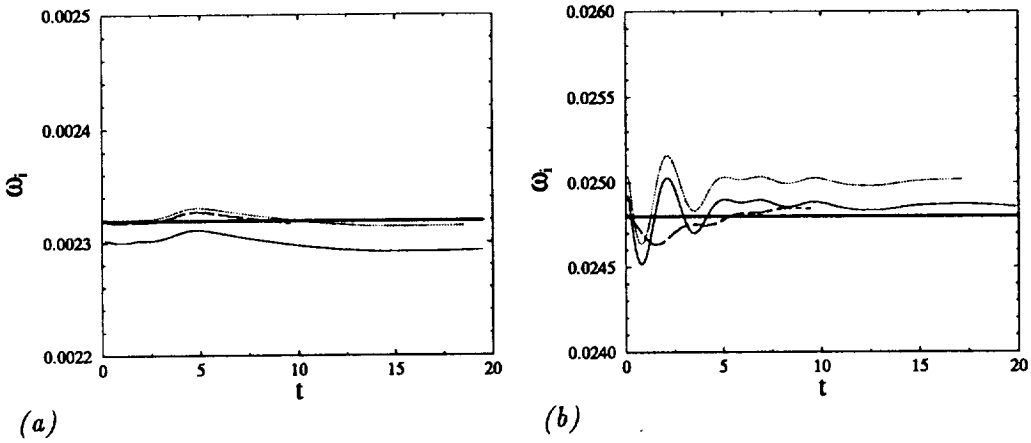

FIGURE 2. Global growth rate. (a) test case A, —— (10 × 10 × 50), ····· (20 × 20 × 50), ---- (20 × 20 × 100), —— (40 × 40 × 100), ▬▬ linear theory. (b) test case B, —— (10 × 50), ····· (20 × 50), ---- (20 × 100), —— (40 × 100), ▬▬ linear theory.

ENO scheme is inactive. We define a modal energy as

$$E(k_x, k_y; t) = \int_0^{L_z} \bar{\rho}(z)\hat{u}_j(k_x, k_y; t)\hat{u}_j^*(k_x, k_y; t)dz \tag{4}$$

u_j stands for the three velocity components (sum over j).

Fig. 2 shows the growth-rate obtained from the modal energy for different discretizations for 1100 time steps each. The initial transient is an effect of different solution methods and different meshes used for the initial eigenmode and for the DNS.

Figs. 3 and 4 show the local growth rate and frequency across the boundary layer for test cases A and B, respectively, making use of the fact that the eigenfunction maintain their shape in a parallel boundary layer. The improvement from a discretization 10 × 50 to 20 × 100 is mainly due to the refinement in z which allows for a better resolution of the region around the critical layer which is also a region of high curvature of the mean-flow profiles.

2.4.2 Eigensolutions of spatially evolving boundary layer

Since the y-discretization remains unchanged compared to the test cases in section 2.4.1, we can restrict ourselves here to 2D-problems. The main concern is the correct formulation of the inflow boundary condition and the efficiency of the outflow-boundary condition given in section 2.3. The test case is the spatially evolving equivalent of case B of section 2.4.1. Also, since it has been found in section 2.4.1 that $N_z = 51$ is about sufficient to resolve the eigenfunctions in z, we focus on the effect of changing N_x and the outflow boundary condition parameters. At the inflow all primitive variables are prescribed (as function of t) according to the

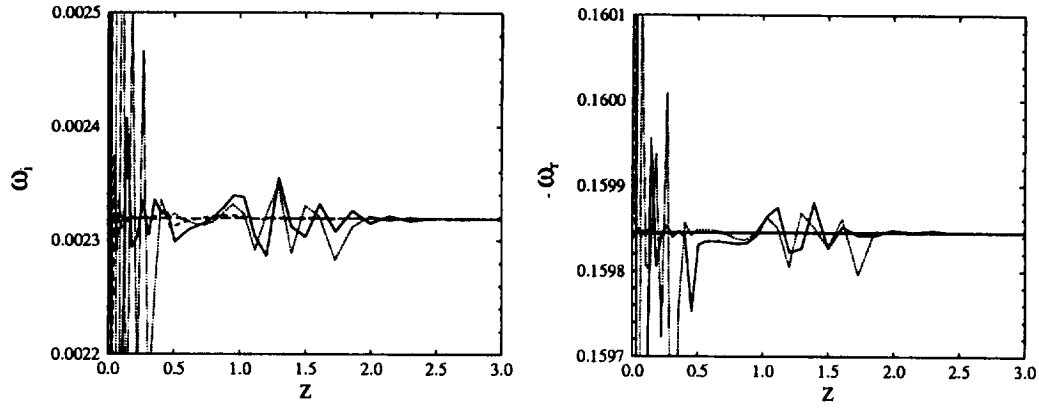

(a) (b)

FIGURE 3. Local growth rate and frequency test case A. (a) growth rate ω_i. (b) frequency ω_r. ——— ρ, (20 × 50), ····· u, (20 × 20 × 50), ---- ρ, (40 × 40 × 100), —— u, (40 × 40 × 100), ▬▬ linear theory.

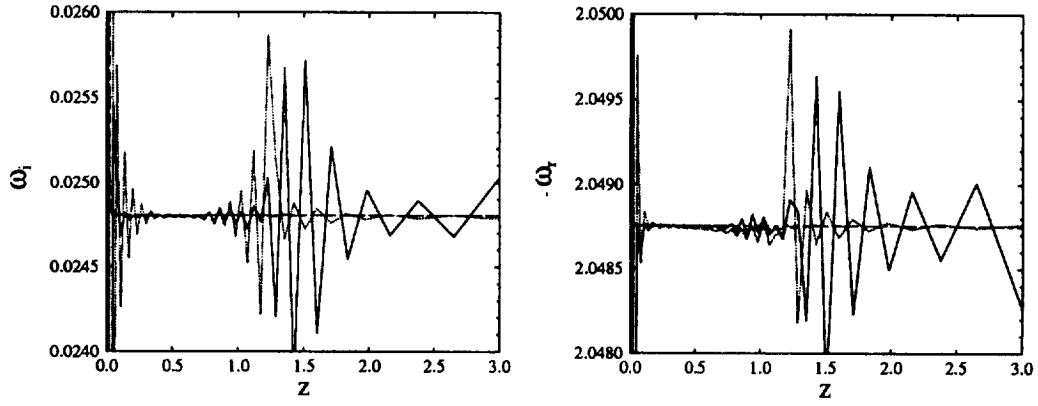

(a) (b)

FIGURE 4. Local growth rate and frequency, test case B, (a) growth rate ω_i. (b) frequency ω_r. ——— ρ, (20), ····· u, (20 × 50), ---- ρ, (40 × 100), —— u, (40 × 100), ▬▬ linear theory.

well-posedness requirement (Oliger & Sundström, 1978); at the outflow the sponge layer of section 2.3 together with a non-reflecting condition at $x = L_x$ is used. As validation-test we check for the correct spatial growth rates in terms of primitive variables at an arbitrary position z. The growth rates are obtained from the coefficients of the solution's Fourier transform in y and t. These coefficients assume the form

$$\hat{a}_{\hat{y}\hat{t}}(x,z) = \hat{A}(z)e^{i\alpha x} \tag{5}$$

where $\hat{A}(z)$ is the complex amplitude function of the linear eigensolution. From two

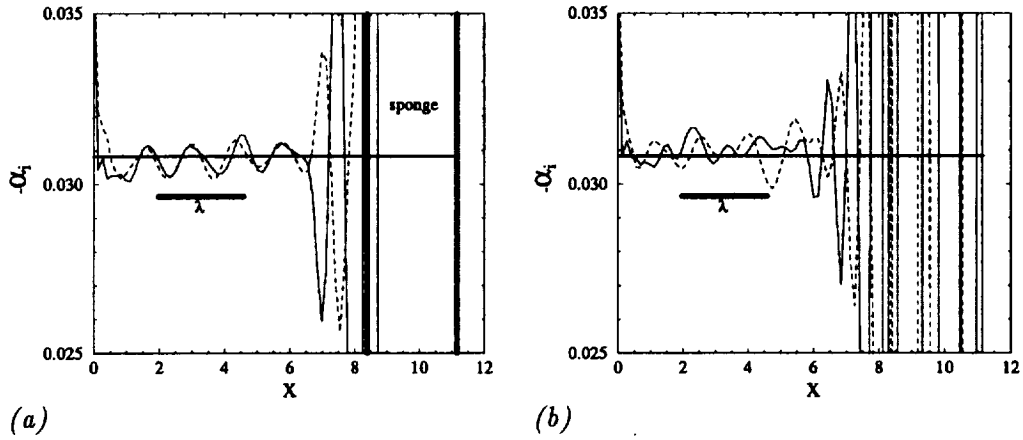

FIGURE 5. Local growth rate, $N_x = 81$, $A_s = 4$, $N_s = 3$, $z = 0.48$, $\delta t = 4\pi/\omega$. (a) sponge layer and non-reflecting boundary condition. (b) non-reflecting boundary condition only. ——— ρ, ---- u, ▬▬ linear theory.

successive x-stations the complex α can then be obtained by

$$\alpha = -i\frac{\ln[\hat{a}_{\hat{y}\hat{i}}(x_2, z)] - \ln[\hat{a}_{\hat{y}\hat{i}}(x_1, z)]}{x_2 - x_1}\,, \tag{6}$$

so that the growth rate is $-\mathrm{Im}(\alpha)$ and the frequency $\mathrm{Re}(\alpha)$.

Fig. 5 shows the effect of the sponge layer. From the experience with a symmetric compact scheme (Guo *et al.*, 1994) we choose the sponge layer thickness to be one wavelength of the eigenmode. The minimum necessary sponge-layer thickness is problem dependent and is therefore not further investigated here. Spurious reflected waves penetrate into the computational domain further upstream in the case of a pure non-reflecting boundary condition, Fig. 5b, than in the case of a non-reflecting boundary condition plus a sponge layer, Fig. 5a. Though this effect is not so pronounced for the low amplitude linear perturbation in the present case, it is expected to be stronger for large amplitude turbulent fluctuations. Note that non-reflecting boundary conditions are not consistent with the evolution of a boundary layer eigensolution. This reflects in large oscillations near the outflow boundary of a sensitive measure as the local growth rate, Fig. 5b.

From Fig. 6 it is evident that increasing the order N_s of the cooling function polynomial in Eq. (3), (making the damping more localized) or increasing the cooling intensity A_s has no noticeable effect on the growth rate or the extent of the valid domain. Thus it is expected that an increased damping is able to extinguish stronger turbulent fluctuation efficiently without increasing the invalid part of the domain.

Fig. 7a shows the same case as Fig. 5a, but the integration time is increased to seven periods so that the wave can travel about two times the width of the computational box. Obviously the region of upstream influence of the boundary

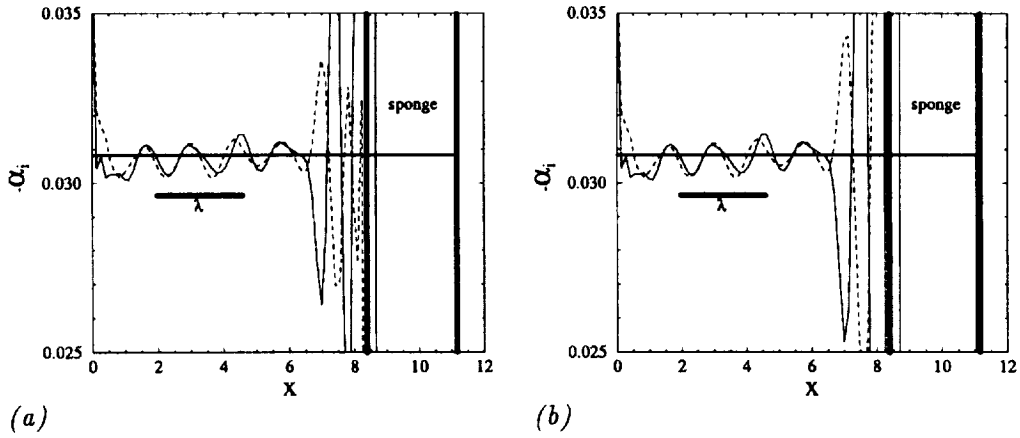

FIGURE 6. Local growth rate, $N_x = 81$, $\delta t = 4\pi/\omega$. (a) $A_s = 4$, $N_s = 7$. (b) $A_s = 10$, $N_s = 3$. —— ρ, ---- u, ▬▬ linear theory.

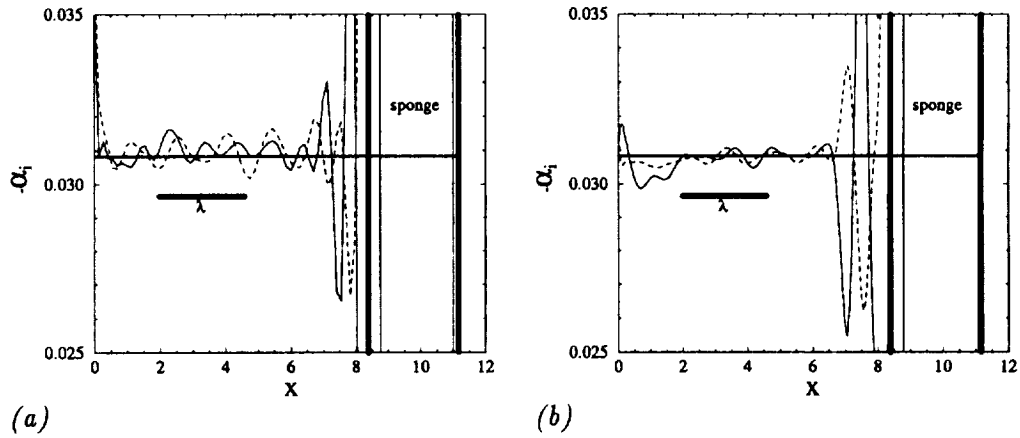

FIGURE 7. Local growth rate. (a) $N_x = 81$, $N_z = 51$, $\delta t = 14\pi/\omega$. (b) $N_x = 161$, $N_z = 101$, $\delta t = 4\pi/\omega$. —— ρ, ---- u, ▬▬ linear theory.

condition did not increase, so that the shorter integration times used before lead to correct conclusions about the upstream extent of the invalid part of the domain. In Fig. 7b both streamwise and vertical number of grid points are doubled, which results in a more accurate approximation of the growth rate as expected.

Two remarks are in order. Firstly we note that the setup used in the above test calculations is quite severe, allowing for only 4 wavelengths λ of the primary wave in x, which finally results in about 2.5λ for the extent of the valid part of the domain. Second, inflow transients are apparently unavoidable (as the initial transients were in the preceding section) since the inflow perturbation is taken from a linear stability solution obtained with a different method and on a different

TABLE 2. Flow parameters.

quantity	value	comment
T^*_∞	221.6K	estimated
M_∞	2	
p^*_∞	9178.79Pa	estimated
Pr	0.72	
κ	1.4	
R	287.03	
μ^*_∞	$1.449 \cdot 10^{-5}$kg/m/s	
S^*	110.4K	
Re_{ξ_0}	140000	
Re_{ξ_1}	450000	
Re_{δ_1}	909.9053	
δ^*_1	$1.5309 \cdot 10^{-4}$m	at ξ_0, from sim. sol.
δ^*_0	$4.7325 \cdot 10^{-4}$m	99.9% thickness
ξ_0	82.7559	
L_x	415	
L_z	200	

mesh. Other DNS results (e.g. Pruett *et al.*, 1994, Guo *et al.*, 1994) confirm this observation.

It can be concluded that the outflow boundary treatment has no upstream effect further than roughly 1.5λ upstream of L_x for $(L_x - x_s) = \lambda$. The findings in this section resemble the experiences made by Guo *et al.*(1994) with a different spatial discretization and a different cooling term. Pruett *et al.*(1994) report that their buffer domain approach spoils an upstream region of about 2λ. The sponge layer approach thus allows for a much simpler formulation with a comparable performance of a well-tuned buffer-domain approach.

2.4.3 Laminar boundary layer interacting with an impinging shock

The following test example is a standard case for the validation of steady state Navier-Stokes solvers. Experimental data are provided by Hakkinen *et al.*(1959). Although the experimental evaluation is limited and the comparison suffers from incompletely reported flow parameters, the experiment's favorable feature is that the flow is laminar, although it should be noted that the test section extends into the region where the laminar flat plate boundary layer is unstable.

An extensive numerical investigation of this particular problem has been done by Katzer (1989). We emphasize here that for the results presented in this section time-accurate and low-dissipation methods have been used. The computations have thus been halted before a true steady state has been reached. The flow parameters are given in table 2 (reference length is δ^*_1, dimensional quantities are marked with a star).

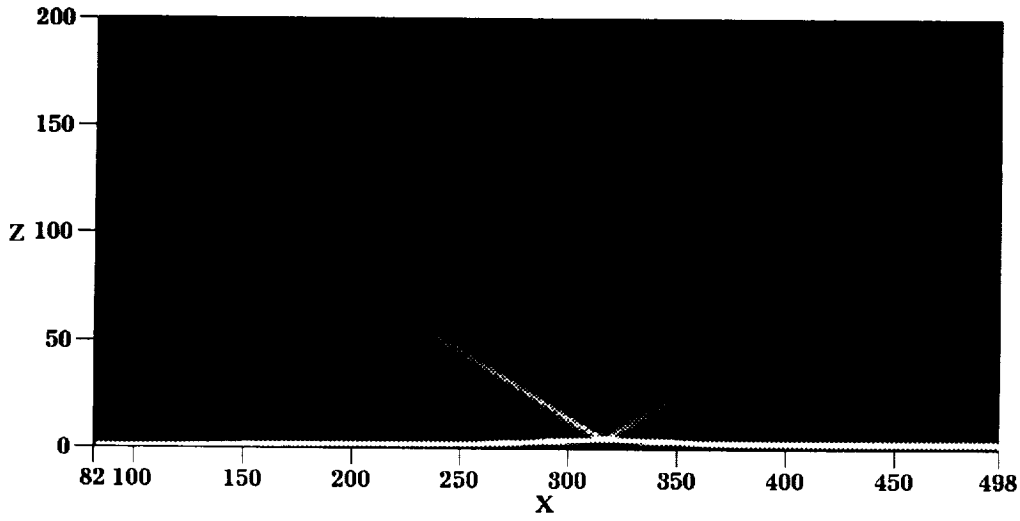

FIGURE 8. Quasi-Schlieren plot (intensity proportional to norm of density gradient).

Fig. 8 shows a quasi-Schlieren plot (merely the norm of the density gradient) when the computations were halted. A shock, introduced at the inflow boundary, impinges at $\beta = 32.6^o$ on the laminar boundary layer along a flat plate. At the boundary layer edge it is reflected as a decompression wave. The shock-induced boundary layer separation gives rise to a compression wave in front of the separation region and a compression wave behind.

As initial condition we take the solution of the inviscid shock-reflection problem outside of the boundary layer, while near the wall a boundary layer from a similarity solution is given. The shock is to impinge on the plate at $x_{sh} = 325.2041$ for the inviscid problem.

As boundary conditions we fix at the inflow the initial condition for all primitive variables (giving the correct number of 5 conditions for the Navier-Stokes equations according to Oliger & Sundström, 1978). At the outflow we prescribe perfectly non-reflecting boundary conditions (Thompson, 1987), and no viscous conditions are imposed. In fact the imposition of weak viscous boundary conditions in terms of derivatives of the viscous fluxes (Poinsot & Lele, 1992) was found to have no effect, while the imposition of boundary conditions in terms of stresses (Dutt, 1988) resulted in an outflow boundary-layer due to the inconsistency between boundary condition and solution. At the wall we prescribe a no-slip adiabatic condition. At the upper boundary all flow variables are prescribed corresponding to the state behind the impinging shock. Non-reflecting conditions at the upper boundary (Thompson, 1987) were found to give rise to a viscous (heat-equation like) instability emerging from the corner between inflow and upper boundary. The reason for that behavior is that the presence of the shock close to the upper boundary at the inflow leads to non-negligible viscous terms near the edge of the computational box, and inflow

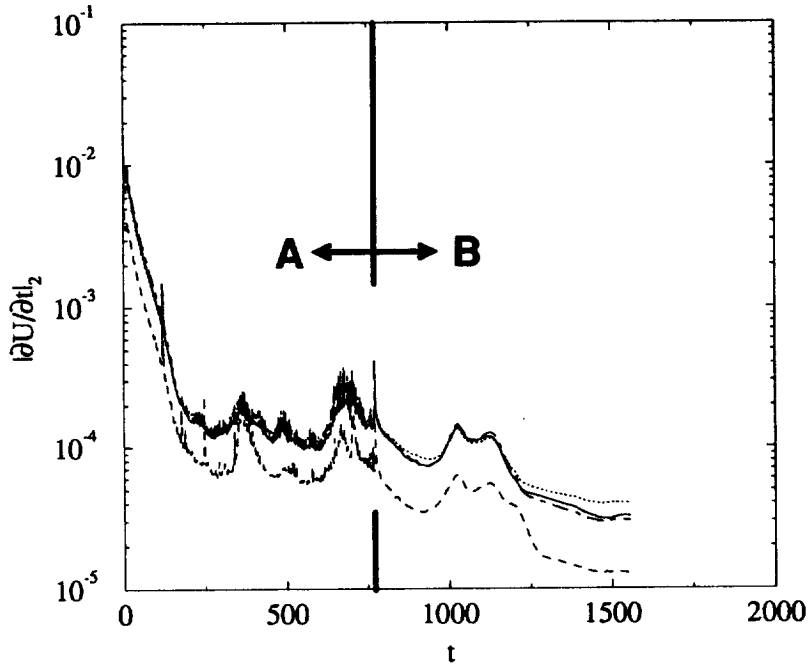

FIGURE 9. Residual. Method A: 3rd order ENO; method B: 5th order hybrid. —— ρ, ····· ρu, ---- ρw, -·- E.

and boundary conditions which are well posed only in the inviscid limit become invalid.

We perform a calculation with $N_x = 151$ and $N_y = 100$. First, the meaningless transient caused by the initial condition is spanned by marching a 3rd order ENO scheme 5500 iterations in time (method A). Note that since we use a time accurate solution procedure and since the ENO-stencil changes in time, the residual does not reach machine zero but merely the truncation error of the spatial discretization. This has been confirmed by continuing the calculation with method A for 5500 additional iterations (not shown). After the residual settled down the computation is continued for another 5500 iterations with the hybrid scheme (method B). Since the Reynolds number is small, the shock is resolvable by the scheme and the ENO-scheme is only active in z in the outer 4.95% of the domain (in the average over all iterations), where the grid spacing is wide (shock detector parameter settings : $\beta_x = 1$, $\beta_z = 0.05$). Fig. 9 shows the evolution of the residual for the four conservative variables.

Figs. 10 and 11 show pressure contours after 5500 iterations with method A and method B, respectively. The hybrid scheme appears to represent the reflected compression and decompression waves more accurately than the pure ENO scheme. This suggests that the internal phenomena of the boundary layer are better represented.

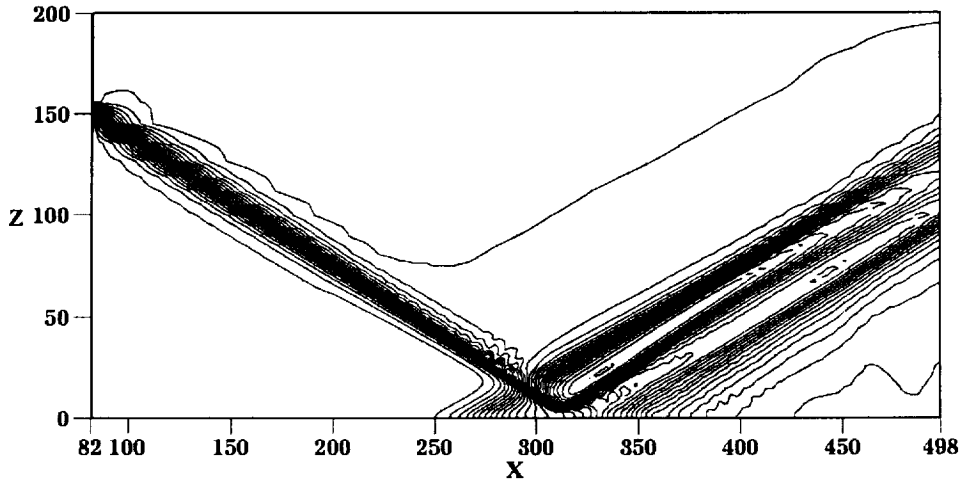

FIGURE 10. Pressure contours after 5500 iterations, method A (min = 0.16, max = 0.26, inc = 0.002).

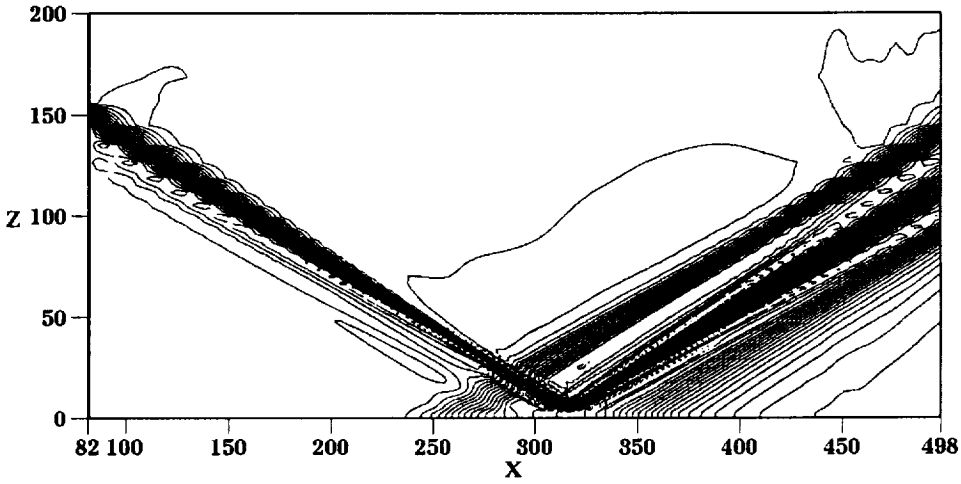

FIGURE 11. Pressure contours after 5500 additional iterations, method B (min = 0.16, max = 0.26, inc = 0.002).

This finding is confirmed if we compare numerical and experimental results. Fig. 12 shows surface pressure and skin friction. In both cases method B gives a better representation. Note that the experimental values downstream of the separation region appear to be affected by the particular method of measuring the skin friction with a pressure probe (Hakkinen, 1959). The accurate numerical solutions of Katzer (1989) show that the experimental values in this region are somewhat too large.

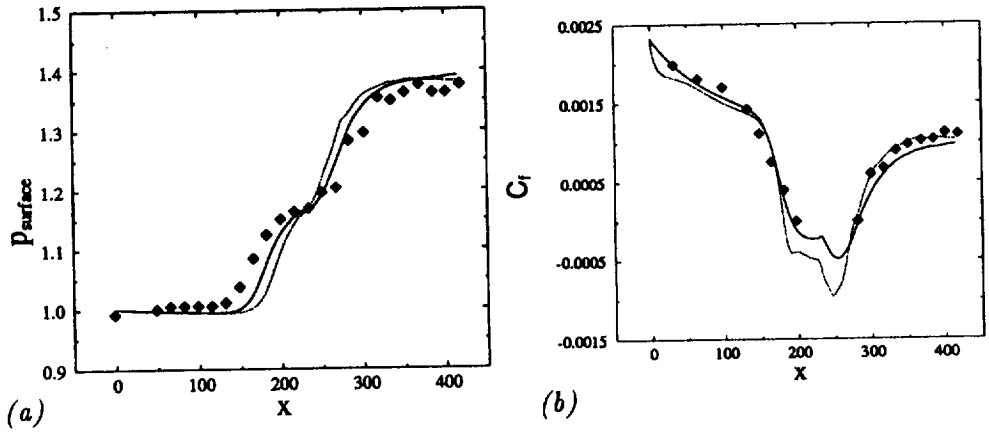

FIGURE 12. Surface pressure (a) and skin friction (b). symbols experiment, ····· after A —— after B.

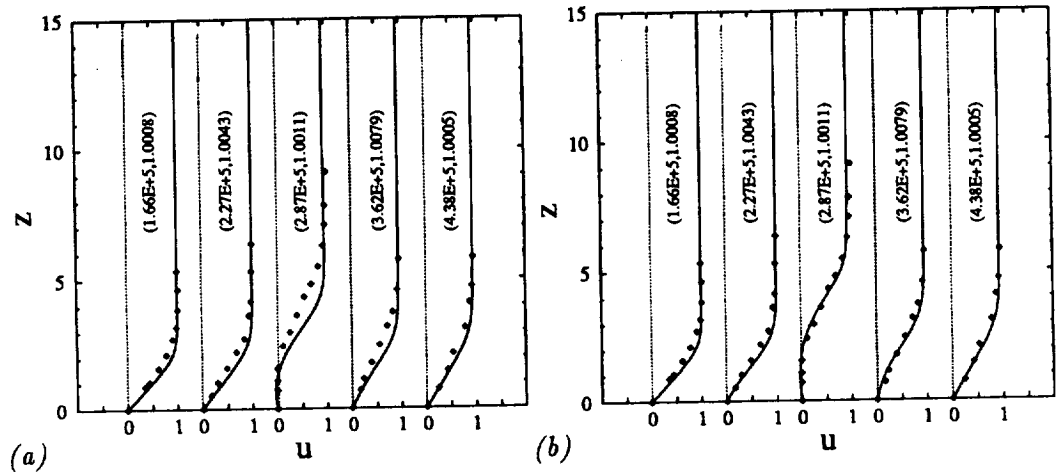

FIGURE 13. Velocity profiles. (a) after A (b) after B. The number-pairs on the curves give Re_{xexp} (first entry) and Re_{xexp}/Re_{xnum} (second entry). symbols experiment, —— computation.

The correspondence between experimentally and numerically obtained velocity profiles is reasonable for method B and less satisfactory for method A, figure 13.

Two remarks are in order. First, as can be seen from Fig. 9, the residual is still decreasing when the computation with method B was halted, though with a shallow slope as expected for a time-accurate method. Thus the results should not be considered as converged. Second, the residual level after the computation with method A was halted does not decrease if the computation is continued with method A. The further decrease of the residual and the improvement of the solution is due to method B.

We finally note that for the present 2D calculations the code performance of the

pure 3rd order ENO scheme was 228 MFLOPS and 143 μs per grid point and time step, while the 5th order hybrid scheme performed at 354 MFLOPS and 23 μs per grid point and time step (CRAY fpp and cft77 optimization only, single processor Y-MP C90).

3. Future plans

In the next step the computational code will be extended to generalized coordinates (in (x, z)). This requires the characteristic transformation routines to be adapted and an extension of the flux calculation routines.

The final objective is to simulate a compression corner flow according to a suitable experiment. Experiments presently considered are those of Smits & Muck (1987) (having the advantage of relatively detailed turbulence data, the disadvantage of a quite large Reynolds number $Re_{\delta_2} = 78000$) of Ardonceau *et al.*(lacking the details of the previous one but having a smaller Reynolds number of roughly $Re_{\delta_2} = 7700$), and of Zheltovodov *et al.*(at about $Re_{\delta_2} = 9720$ for the incoming boundary layer with the problem that mean flow and turbulence data have been obtained in different wind tunnels). The Mach number range of those experiments is between 2.25 and 3, the turning angles go from 8^o to 25^o.

Acknowledgments

I acknowledge the preparatory work of K. Shariff, NASA ARC, concerning hybrid schemes, and his help by reviewing a draft of this report. For graphics postprocessing the package COMADI by H. Vollmers, DLR Göttingen, has been used.

REFERENCES

ADAMS, N. A. 1993 Numerische Simulation von Transitionsmechanismen in kompressiblen Grenzschichten. *Doctoral Dissertation,* Technical University of Munich, Germany. Also *DLR-FB* 93-29, DLR, Germany (in German).

ADAMS, N. A. & SHARIFF, K. 1994 A high-resolution hybrid compact-ENO scheme for shock-turbulence interaction problems. *CTR Manuscript* in preparation.

ANDERSON, D. A., TANNEHILL, J. C. & PLETCHER, R. H. 1984 *Computational Fluid Mechanics and Heat Transfer.* Hemipshere Publ. Corp., New York.

ANDREOPOULOS, J. & MUCK K. C. 1987 Some new aspects of the shock-wave / boundary-layer interaction in compression-ramp flows. *J. Fluid Mech.* **180. 405-428.**

ARDONCEAU, P., LEE, D. H., ALZIARY DE ROQUEFORT, T. & GOETHALS, R. 1979 Turbulence behavior in shock wave / boundary layer interaction. *AGARD CP-271*, paper 8.

COCKBURN, B. & SHU, C.-W. 1994 Nonlinearly stable compact schemes for shock calculations. *SIAM J. Numer. Anal.* **31,** 607–627.

DUTT, P. 1988 Stable boundary conditions and difference schemes for Navier-Stokes equations. *SIAM J. Numer. Anal.* **25,** 245–267.

GUO, Y. & ADAMS, N. A. 1994 Numerical investigation of supersonic turbulent boundary layers with high wall temperature. *Proc. 1992 Summer Program,* CTR, Stanford Univ. - NASA ARC.

GUO, Y., KLEISER, L. & ADAMS, N. A. 1994 A comparison study of an improved temporal DNS and spatial DNS of compressible boundary layer transition. *AIAA-paper* 94-2371 (sub. to *AIAA Journal*).

GUSTAFSSON, B. 1975 The convergence rate of difference approximations to mixed initial boundary value problems. *Math. Comput.* **29,** 396–406.

HAKKINEN, R. J., GREBER, I., TRILLING, L. & ABARBANEL, S. S. 1959 The interaction of an oblique shock wave with a laminar boundary layer. *NASA Memorandum* 2-18-59W.

HOU, T. Y. & LE FLOCH, P. G. 1994 Why nonconservative schemes converge to wrong solutions: error analysis. *Math. Comput.* **62,** 497–530.

ISRAELI, M. & ORSZAG, S. A. 1981 Approximation of radiation boundary conditions. *J. Comp. Phys.* **41,** 115–135.

KATZER, E. 1989 On the length scales of laminar shock/boundary-layer interaction. *J. Fluid Mech.* **206,** 477–496.

KLINE, S. J., CANTWELL, B. J. & LILLEY, G. M. (EDS) 1981 *Proc. 1980-81 AFOSR-HTTM Stanford Conf. Complex Turbul. Flow, Vol. III.* Thermosci. Div., Stanford Univ., CA.

KLOKER, M., KONZELMANN, U. & FASEL, H. 1993 Outflow boundary conditions or spatial Navier-Stokes simulations of transition boundary layers. *AIAA Journal* **31**, pp. 620–628.

LEE, S. S. 1993 Effects of shock strength on shock turbulence interaction. In *Annual Research Briefs - 1993.* CTR, Stanford Univ. - NASA ARC, 329-345.

LELE, S. K. 1992 Compact finite difference schemes with spectral-like resolution. *J. Comp. Phys.* **103**, 16-42.

MACK, L. M. 1984 Boundary-layer stability theory. In *Special Course on Stability and Transition of Laminar Flow.* AGARD Rep. No. 709, 3-1–3-81.

OLIGER, J. & SUNDSTRÖM, A. 1978 Theoretical and practical aspects of some initial boundary value problems in fluid dynamics. *SIAM J. Appl. Math.* **35**, 419–446.

POINSOT, T. J. & LELE, S. K. 1992 Boundary conditions for direct simulations of compressible viscous flows. *J. Comp. Phys.* **101**, 104–129.

PRUETT, C. D., ZANG, T. A., CHANG, C.-L. & CARPENTER, M. H. 1994 Spatial direct numerical simulation of high-speed boundary-layer flows – part I: algorithmic considerations and validation. *Theor. Comput. Fluid Dyn.* **6.**

RAI, M. M. & MOIN, P. 1993 Direct numerical simulation of transition and turbulence in a spatially evolving boundary layer. *J. Comp. Phys.* **109**, 169–192.

SHU, C.-W. 1988 Total-variation-diminishing time discretizations. *SIAM J. Sci. Stat. Comput.* **9**, 1073–1084.

SHU, C.-W., & OSHER, S. 1989 Efficient implementation of essentially non-oscillatory shock-capturing schemes. II. *J. Comp. Phys.* **83**, 32–78.

SIMEN, M. 1993 Lokale und nichtlokale Instabilität hypersonischer Grenzschichtströmungen *Doctoral Dissertation,* University of Stuttgart, Germany. Also *DLR-FB* 93-31, DLR, Germany (in German).

SMITS, A. J. & MUCK, K.-C. 1987 Experimental study of three shock wave / turbulent boundary layer interactions. *J. Fluid Mech.* **182**, 291-214.

STEWARTSON, K. 1964 *The Theory of Laminar Boundary Layers in Compressible Fluids.* Oxford University Press, London.

THOMPSON, K. W. 1987 Time dependent boundary conditions for hyperbolic systems. *J. Comput. Phys.* **68**, 1–24.

WILLIAMSON, J. H. 1980 Low-storage Runge-Kutta schemes. *J. Comp. Phys.* **35**, 48–56.

ZHELTOVODOV, A. A., ZAYLICHNY, E. G., TROFIMOV, V. M. & YAKOVLEV, V. N. 1990 An experimental documentation of supersonic turbulent flows in the vicinity of sloping forward and backward facing steps. In Settles, G. S., & Dodson, L. J. 1994 Supersonic and hypersonic shock / boundary-layer interaction database. *AIAA Journal* **32**, 1377–1383.